Available online at www.sciencedirect.com

ScienceDirect

Ceramics International 42 (2016) 5461–5471

CERAMICS INTERNATIONAL

www.elsevier.com/locate/ceramint

Design and synthesis of metal oxide hollow nanopowders for lithium-ion batteries by combining nanoscale Kirkendall diffusion and flame spray pyrolysis

Jong Min Won[a], Jong Hwa Kim[b], Yun Ju Choi[c], Jung Sang Cho[a], Yun Chan Kang[a,*]

[a]*Department of Materials Science and Engineering, Korea University, Anam-Dong, Seongbuk-Gu, Seoul 136-713, Republic of Korea*
[b]*Daegu Center, Korea Basic Science Institute, 80 Daehakro Bukgu, Daegu 702-701, Republic of Korea*
[c]*Suncheon Center, Korea Basic Science Institute, Suncheon 540-742, Republic of Korea*

Received 17 October 2015; received in revised form 15 December 2015; accepted 17 December 2015
Available online 28 December 2015

Abstract

This study introduces an efficient process that combines a gas phase reaction method and nanoscale Kirkendall diffusion for the large-scale production of metal-oxide hollow nanopowders. Core-shell-structured NiO@SiO_2 nanopowders prepared by flame spray pyrolysis are transformed into hollow NiO@SiO_2 nanopowders via a nanoscale Kirkendall diffusion process. The SiO_2 coating layer plays a key role in preventing the sintering and growth of the Ni or NiO nanopowders during the preparation process. The mean size of hollow core and shell thickness of the hollow NiO nanopowders are 11 and 7 nm, respectively. At a current density of 0.5 A g^{-1}, the NiO@SiO_2 nanopowders with hollow and filled structures exhibit 100th cycle discharge capacities of 885 and 338 mA h g^{-1}, respectively. In addition, the hollow NiO@SiO_2 nanopowders, which exhibit low charge transfer resistances and fast Li-ion diffusion rates, also show better cycling and rate performance than the nanopowders with filled structures.

Keywords: Kirkendall diffusion; Nickel oxide; Lithium ion battery; Flame spray pyrolysis

1. Introduction

Hollow-structured metal-oxide nanopowders can be used in various applications including energy storage materials, solar cells, catalysts, sensors, and drug delivery systems [1–6]. Therefore, various chemical processes have been developed to produce these nanopowders [7–10]. Recently, conversion chemical reactions, such as nanoscale Kirkendall diffusion, anion exchange, and galvanic exchange, have received significant attention for the production of hollow nanopowders [11–17]. In the nanoscale Kirkendall diffusion and anion exchange processes, nanovoids form within the nanoparticles when the outward diffusion of species from the nanoparticle core is more rapid than the inward diffusion of reactive species; i.e., nanovoid formation is driven by a difference in diffusion rates [13–17].

Today, conversion chemical reactions are used to develop transition-metal-oxide hollow nanopowders as anode materials to prepare rechargeable Li-ion batteries (LIBs) with excellent electrochemical properties [17–27]. Compared with their filled structure counterparts, metal-oxide hollow nanopowders have a shorter Li-ion diffusion length and better accommodate the volume changes resulting from repeated insertion and extraction of Li [17–18,20–27]. Metal-oxide hollow nanopowders obtained via the nanoscale Kirkendall diffusion process have mainly been developed using liquid solution processes [11–13,28–32]. In addition, metal-oxide hollow nanopowders with uniform size distribution and pore volume have been successfully prepared via a controlled oxidation process under liquid media of the metal nanopowders; these liquid media were formed by liquid solution processes, such as hydrothermal and precipitation

---

[*] Corresponding author.
E-mail address: yckang@korea.ac.kr (Y.C. Kang).

http://dx.doi.org/10.1016/j.ceramint.2015.12.092
0272-8842/© 2016 Elsevier Ltd and Techna Group S.r.l. All rights reserved.

processes [19–22,33]. In fact, sintering and particle growth of the metal nanopowders before the nanoscale Kirkendall diffusion process hinders the preparation of non-aggregated metal-oxide hollow nanopowders by simple oxidation under air atmosphere. Thus, the development of a new simple process for synthesizing hollow nanopowders remains challenging.

Flame spray pyrolysis, a gas phase reaction method, was developed for the large-scale production of nanosized ceramic, metal, and metal-ceramic composite powders [34–36]. However, reducing atmospheres are unsuitable in flame spray pyrolysis. Therefore, nanopowders containing precious metals, such as Ag, Pd, Au, and Pt, which can be prepared in air, have been prepared by flame spray pyrolysis [37–40]. To the best of our knowledge, the preparation of transition-metal-oxide nanopowders with hollow structures using flame spray pyrolysis has never been studied.

In this study, for the first time, a simple and efficient process for the metal-oxide hollow nanopowders via combined gas phase reaction and nanoscale Kirkendall diffusion processes was introduced. The core–shell-structured metal oxide@silica nanopowders were prepared by one-pot flame spray pyrolysis from vapors of Si and metal components. The metal oxide@silica nanopowders were subjected to a reduction process, and hollow metal oxide@silica nanopowders were formed after subsequent oxidation under an air atmosphere via the nanoscale Kirkendall diffusion process. In this study, anode materials for LIBs were successfully prepared from NiO hollow nanopowders using this newly developed process, and the electrochemical properties of these nanopowders were compared with those of filled NiO@SiO_2 nanopowders.

2. Experimental

NiO@SiO_2 nanopowders were prepared using a flame spray pyrolysis system that consists of a droplet generator, flame nozzle, powder collector, and blower [40,41]. A 1.7-MHz ultrasonic spray generator with 6 resonators was used to generate droplets, which were carried into the high-temperature diffusion flame by oxygen, the carrier gas. Propane and oxygen were used as the fuel and oxidizer, respectively, to create the diffusion flame. The flame nozzle consisted of 5 concentric pipes. Droplets generated from the precursor solution were supplied to the diffusion flame by the carrier gas flowing through the center pipe. The flow rates of the fuel, oxidizer, and carrier gas were 8, 85, and 9 L min^{-1}, respectively.

The spray solutions were obtained by adding nickel nitrate ($Ni(NO_3)_2$, Junsei, 97%), and tetraethyl orthosilicate ($Si(OC_2H_5)_4$, Samchun, 98%). A small amount of nitric acid was added to form the clear spray solution. The volume ratio of ethyl alcohol/distilled water in the mixed solvent was 1/3. Ethyl alcohol was added to increase the temperature of the diffusion flame. The overall concentration of the Ni and Si components was fixed at 0.08 M. In addition, the NiO@SiO_2 nanopowders obtained from the pyrolysis were reduced at 500 °C under a 10% H_2/Ar reducing atmosphere to produce the Ni@SiO_2 nanopowders. Hollow NiO nanopowders were subsequently produced by oxidizing the Ni@SiO_2 nanopowders at 300 °C for 10, 30, 60, and 180 min under an air atmosphere.

The microstructures of the powders were examined using field-emission scanning electron microscopy (FE-SEM, Hitachi, S-4800) and field-emission transmission electron microscopy (FE-TEM, JEOL, JEM-2100F). In addition, the constituent crystal phases were determined by X-ray diffraction (XRD, X'Pert PRO MPD) using Cu Kα radiation ($\lambda = 1.5418$ Å) at the Korea Basic Science Institute (Daegu). X-ray photoelectron spectroscopy (XPS, Thermo Scientific K-Alpha) with a focused monochromatic Al Kα at 12 kV and 20 mA was used to analyze the composition of the specimens. The surface area of the powders was determined using the Brunauer–Emmett–Teller (BET) method, with N_2 as the adsorbate gas.

The electrochemical properties of the powders were analyzed by constructing a 2032-type coin cell. The anode was prepared by mixing the NiO@SiO_2 nanopowders, carbon black, and sodium carboxymethyl cellulose (CMC) in a weight ratio of 7:2:1. Li metal, microporous polypropylene film, and 1 M $LiPF_6$ dissolved in a mixture of ethylene carbonate/dimethyl carbonate (FEC/DMC; 1:1 v/v) were used as the counter electrode, separator, and electrolyte, respectively. The discharge/charge characteristics of the samples were investigated by cycling in the potential range of 0.001–3 V at various current densities. Cyclic voltammogram (CV) curves were obtained at a scan rate of 0.07 mV s^{-1}. The dimensions of the negative electrode were 1 cm × 1 cm, and the mass loading of the active materials was approximately 1.2 mg cm^{-2}. Furthermore, electrochemical impedance spectroscopy (EIS) was performed at frequencies ranging from 100 kHz to 0.01 Hz.

3. Results and discussion

The formation mechanism of the hollow NiO@SiO_2 nanopowders produced via the nanoscale Kirkendall diffusion process is shown in Scheme 1. The core-shell-structured NiO@SiO_2 nanopowders with filled structures were prepared by high-temperature flame spray pyrolysis from the vapors of SiO_2 and nickel oxide, as described in our previous publication [41]. The Ni@SiO_2 nanopowders with filled structure were produced by post-treating the NiO@SiO_2 nanopowders under a reducing atmosphere. Subsequent oxidation under an air atmosphere produced the hollow NiO@SiO_2 nanopowders via the nanoscale Kirkendall diffusion process. After the formation of the thin NiO layer, small Ni cations (radius = 83 pm) diffused outward from the boundary between the Ni and NiO layers to the surface of the Ni/NiO (core/shell) nanocrystals faster than the large oxygen anions (radius = 140 pm) could diffuse inward [42]. The complete conversion of Ni into NiO via the nanoscale Kirkendall diffusion transformed the Ni single nanocrystals into polycrystalline NiO hollow nanospheres. In addition, the silica coating layer played a key role in preventing the sintering and growth of the metal or metal-oxide nanopowders during the second step of the post-treatment process. The reduction of bare NiO nanopowders resulted in large-sized Ni powders with irregular morphology.

The formation mechanism of the hollow NiO@SiO$_2$ nanopowders was investigated based on post-treatment-induced morphology changes in the NiO@SiO$_2$ nanopowders. Fig. 1 shows the morphologies of the nanopowders, which were prepared by high-temperature flame spray pyrolysis. The TEM image shown in Fig. 1a revealed the nanometer size of the powder. Furthermore, the high-resolution TEM images shown in Fig. 1b revealed the core-shell structure of the NiO@SiO$_2$ composite nanopowders. The NiO nanocrystals with clearly visible 0.24-nm-spaced lattice fringes, corresponding to the (111) crystal plane of cubic NiO, were uniformly covered with amorphous-like material, as indicated by the arrows. As reported in our previous publication, the core-shell-structured NiO@SiO$_2$ nanopowders were prepared directly by flame spray pyrolysis from the vapors of NiO and SiO$_2$ [41]. The drying and decomposition of droplet containing Ni(NO$_3$)$_2$ and tetraethyl orthosilicate inside the diffusion flame formed the micron-sized NiO–SiO$_2$ composite powder. Complete evaporation of the NiO–SiO$_2$ composite powders inside the diffusion flame at temperatures above 2500 °C produced the vapors of NiO and SiO$_2$. The NiO–SiO$_2$ composite nanopowders were formed at the exit part of the diffusion flame by nucleation and growth mechanism. The core–shell structure resulted from the growth of NiO nanocrystals inside the NiO@SiO$_2$ composite nanopowder [41]. The growth of NiO crystals inside the NiO–SiO$_2$ composite nanopowder gathered the Ni component to form the core. The amorphous SiO$_2$ migrated to the surface of the nanopowder to form the shell layer. Moreover, elemental mapping images (Fig. 1c) revealed that the Ni and Si components were uniformly distributed in the NiO@SiO$_2$ composite nanopowders.

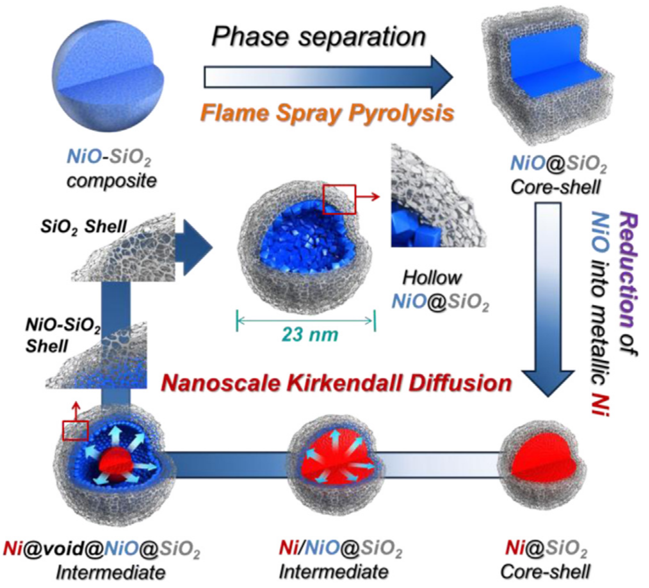

Scheme 1. Schematic diagram showing the formation mechanism of the hollow NiO@SiO$_2$ nanopowders via the nanoscale Kirkendall diffusion process.

Fig. 2 shows the morphologies of the Ni@SiO$_2$ composite powders formed during the reduction process of the core–shell NiO@SiO$_2$ nanopowders at 500 °C. During the reduction and melting process, the well-faceted NiO nanopowders transformed into spherical-like Ni nanopowders, which were uniformly covered with an amorphous SiO$_2$ layer. The inset

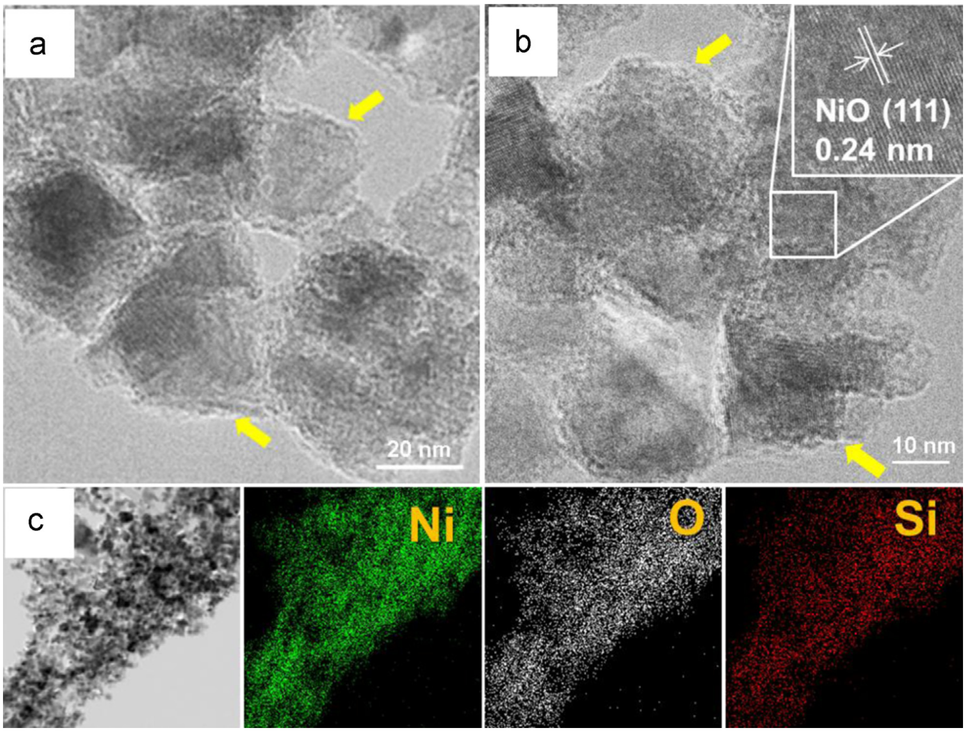

Fig. 1. Morphologies and elemental mapping images of the NiO@SiO$_2$ nanopowders prepared by flame spray pyrolysis: (a) and (b) TEM images, and (c) elemental mapping images.

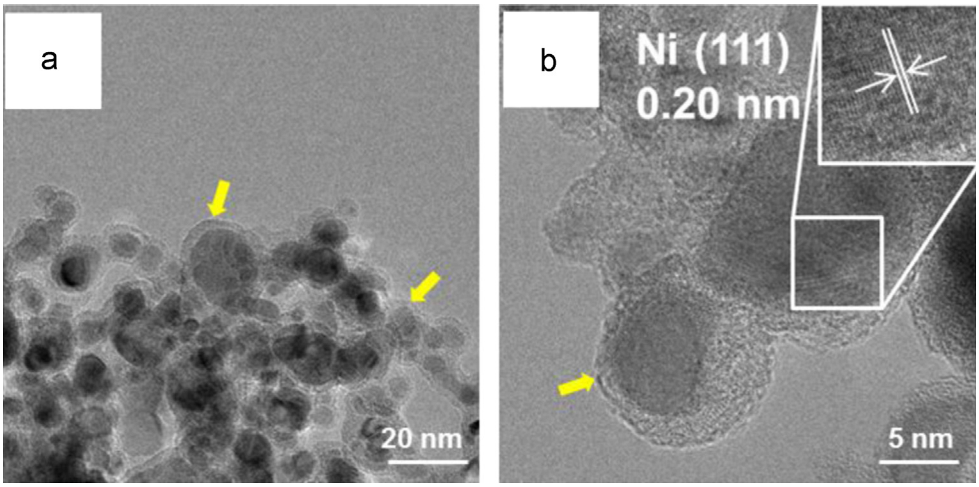

Fig. 2. TEM images of the Ni@SiO_2 nanopowders post-treated at 500 °C in 10% H_2/Ar atmosphere for 3 h: (a) low resolution and (b) high resolution..

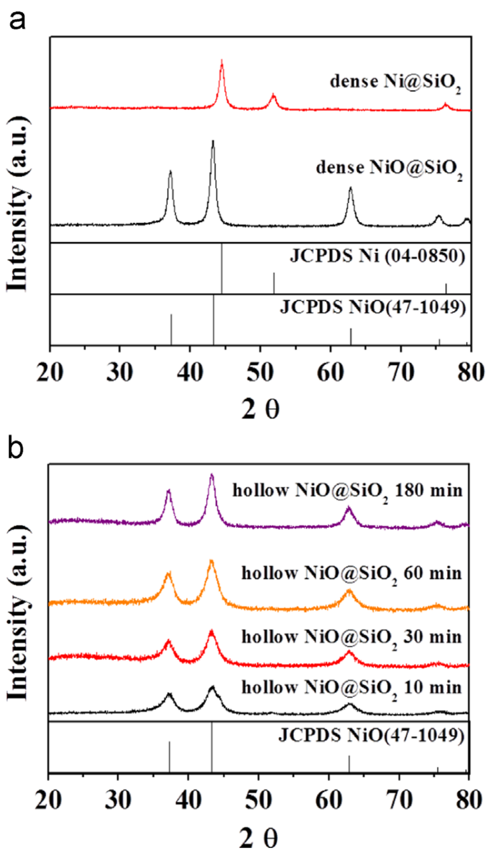

Fig. 3. XRD patterns of the nanopowders (a) filled NiO@SiO_2 and Ni@SiO_2 nanopowders before Kirkendall diffusion process, and (b) hollow NiO@SiO_2 nanopowder second-step post-treated at various oxidation times.

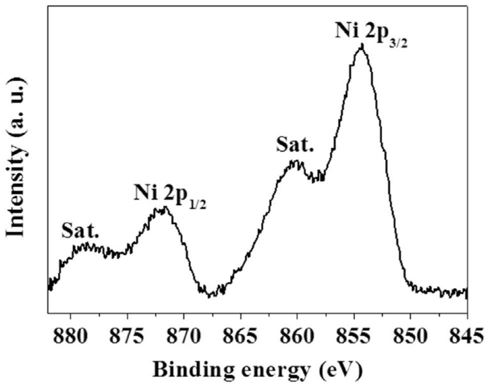

Fig. 4. XPS spectrum of hollow NiO@SiO_2 nanopowders second-step post-treated at 300 °C in air for 180 min.

image in Fig. 2b reveals clear 0.20-nm-spaced lattice fringes, which correspond to the (111) crystal plane of metallic Ni. The mean size of the Ni nanopowders in the high-resolution TEM images was measured to be 9.4 nm. In addition, the SiO_2 coating layer effectively disrupted the crystal growth and aggregation of the Ni nanopowders, as evidenced by the lack of necking between the Ni nanopowders during the reduction process at 500 °C. The XRD patterns (Fig. 3a) of the nanopowders obtained before and after reduction process at 500 °C revealed that NiO was completely reduced into metallic Ni during the reduction process. Ni in the Ni@SiO_2 nanopowders had a mean crystallite size of 11.5 nm, as calculated from the width of the (111) peak using the Scherrer equation; this mean crystallite size is similar to that determined from the TEM image. Therefore, the Ni nanopowders covered by the amorphous SiO_2 layer observed in Fig. 2 were single crystals.

Changes in the morphology and crystal structure of the Ni@SiO_2 nanopowders under an air atmosphere at 300 °C were investigated as a function of the oxidation time. The XRD patterns (Fig. 3b) revealed that metallic Ni oxidized into NiO within 10 min, thereby forming the NiO@SiO_2 nanopowders. This oxidation was further confirmed by the XPS spectrum (Fig. 4) of Ni 2p. The XPS spectrum revealed two main peaks at binding energies of 855.9 eV for Ni $2p_{3/2}$ and 873.4 eV for Ni $2p_{1/2}$ with two shakeup satellites (denoted as "Sat."), which are the characteristic peaks of NiO. Furthermore, the mean crystallite sizes of NiO in the NiO@SiO_2 nanopowders were calculated from the width of the (200) peak using the Scherrer equation. The mean crystallite size increased with increasing oxidation time, and values of 3.8, 4.4, 5.0, and 7.6 nm were obtained for times of 10, 30, 60, and 180 min,

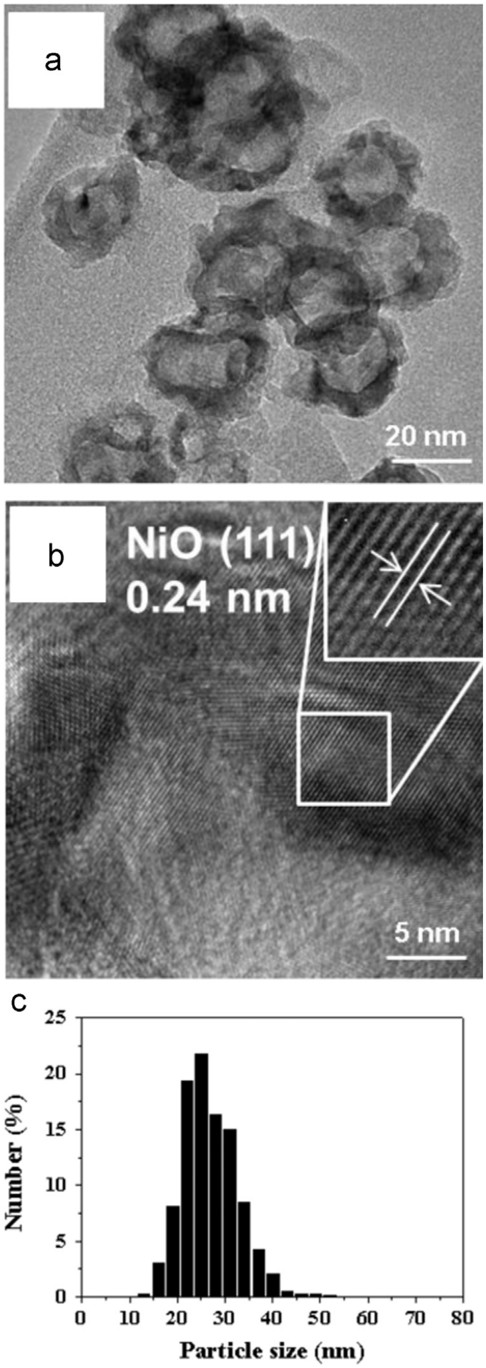

Fig. 5. Morphologies and particle size distribution of the hollow NiO@SiO_2 nanopowders obtained at oxidation time of 180 min: (a) low resolution TEM image, (b) high resolution TEM image, and (c) particle size distribution.

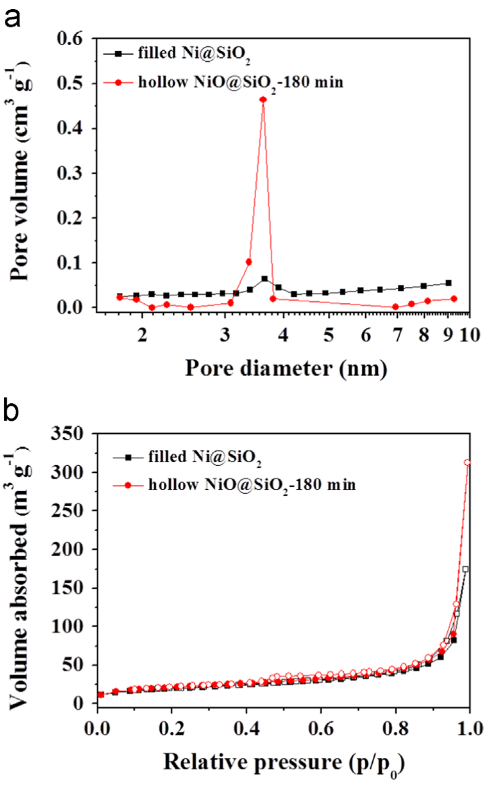

Fig. 6. N_2 adsorption and desorption isotherms and pore size distributions of filled Ni@SiO_2 and hollow NiO@SiO_2 nanopowders second-step post-treated at 300 °C in air for 180 min.

respectively. Fig. 5 shows the morphologies of the NiO@SiO_2 nanopowders obtained after 180 min of oxidation. This prolonged oxidation transformed the Ni@SiO_2 nanopowders with filled structures into hollow NiO@SiO_2 nanopowders and converted the Ni nanocrystals into hollow NiO nanospheres via the Kirkendall effect. The 0.24-nm-spaced clear lattice fringes observed in the inset of Fig. 5b correspond to the (111) plane of the cubic NiO phase. A mean size of hollow core and mean shell thickness of 11 and 7 nm, respectively, were measured from the high-resolution TEM images of the hollow NiO nanopowders; i.e., the second step of the post-treatment transformed the filled NiO nanopowders, which have a mean size of 8.7 nm, into hollow NiO nanopowders with a mean size of 25 nm. The size distribution of the hollow NiO@SiO_2 nanopowders measured from the TEM images is shown in Fig. 5c. The N_2 adsorption and desorption isotherms and Barrett–Joyner–Halenda (BJH) pore size distribution of the hollow NiO@SiO_2 nanopowders are presented in Fig. 6. These nanopowders contained mesopores with a pore diameter of 3.5 nm at the peak of the distribution and a BET surface area of 75 m^2 g^{-1}. Furthermore, elemental mappings of the Ni@SiO_2 and NiO@SiO_2 nanopowders before and after the nanoscale Kirkendall diffusion process (Fig. 7) revealed slight phase separations of the Si and Ni components in both samples. This finding indicates that slight segregation of the amorphous SiO_2 layers occurred during the post-treatment process.

The morphologies of the NiO@SiO_2 nanopowders obtained after oxidation for 30 min are shown in Fig. 8. Fig. 8 reveals that the Ni single nanocrystals transformed completely into polycrystalline NiO hollow nanospheres after only 30 min of oxidation. The inset image in Fig. 8a reveal clear 0.24-nm-spaced lattice fringes, which correspond to the (111) crystal plane of cubic NiO. However, high-resolution TEM image (Fig. 8b) revealed that the NiO hollow nanospheres exhibited poor crystallinity. The XRD patterns (Fig. 3) also revealed the

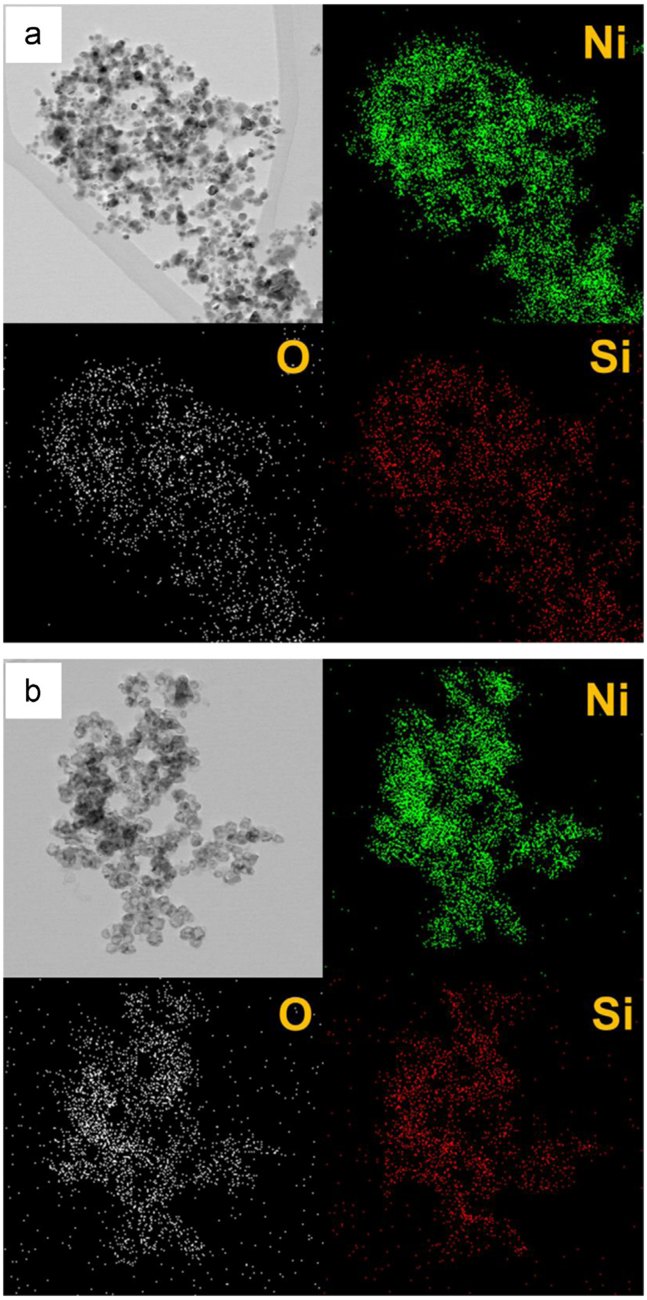

Fig. 7. Elemental mapping images of nanopowders. (a) filled Ni@SiO_2, and (b) hollow NiO@SiO_2 nanopowders second-step post-treated at 300 °C in air for 180 min.

poor crystallinity of the NiO@SiO_2 nanopowders formed via the nanoscale Kirkendall diffusion process during short oxidation. Metallic Ni was completely converted into NiO after only 10 min of oxidation. However, the amorphous SiO_2 coating layer disrupted the crystal growth of NiO formed by the nanoscale Kirkendall diffusion process. The mean crystallite size of the NiO hollow nanospheres increased with the gradual crystal growth of NiO with increasing oxidation time.

The electrochemical properties of the hollow NiO@SiO_2 nanopowders obtained via the nanoscale Kirkendall diffusion process at various oxidation times were compared with those of the NiO@SiO_2 nanopowders with filled structures. Fig. 9 presents CV curves of the four samples; the initial three cycles obtained at a scan rate of 0.07 mV s^{-1} in the potential range of 0.001–3.0 V are shown. During the initial discharge process, the CV curve of the NiO@SiO_2 nanopowders with filled structures exhibited a distinct peak near 0.44 V, which results from the reduction of NiO into metallic Ni and the formation of amorphous Li_2O [43]. The additional reduction peak at ~0.7 V, as indicated by the arrow in Fig. 9a, resulted from the reaction of the amorphous SiO_2 coating layer with Li ions to produce Si through $Li_2Si_2O_5$ [44–46]. In the second and third cycles, the main reduction peaks shifted to high potentials because of the conversion of NiO nanocrystals into amorphous

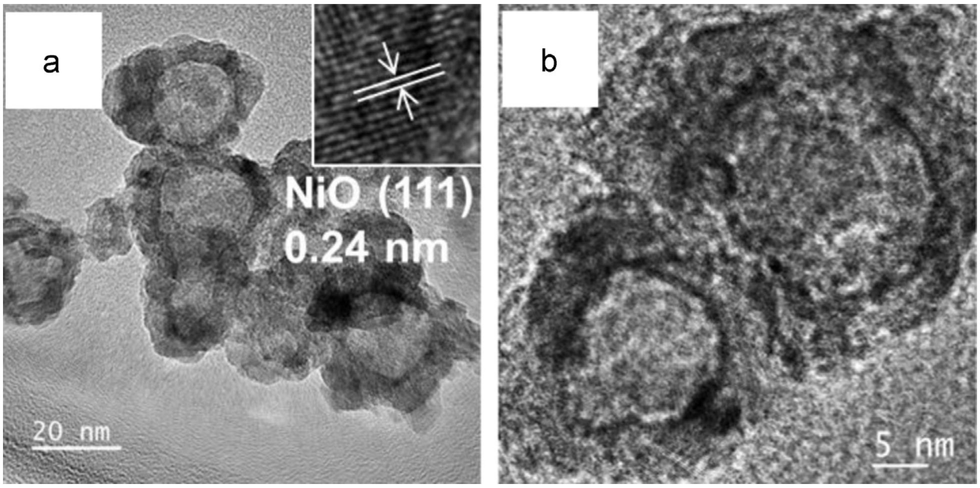

Fig. 8. TEM images of hollow NiO@SiO_2 nanopowders second-step post-treated at 300 °C in air for 30 min: (a) low resolution and (b) high resolution.

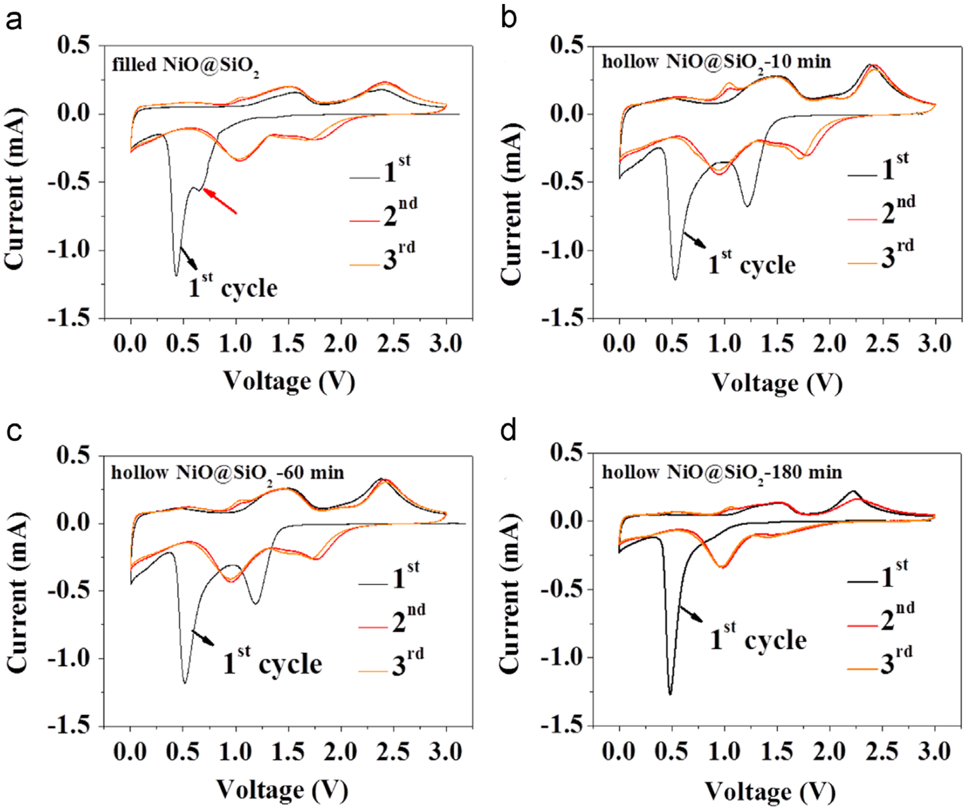

Fig. 9. CV curves of the filled and hollow NiO@SiO_2 nanopowders: (a) filled NiO@SiO_2 nanopowders and (b–d) hollow NiO@SiO_2 nanopowders obtained at oxidation times of 10, 60, and 180 min.

Ni metal during the first cycle. In addition, the CV curves of the hollow NiO@SiO_2 nanopowders obtained at oxidation times of 10 and 60 min exhibited two distinct reduction peaks during the initial discharge process. The broad reduction peak near 0.52 V is attributed to the reduction of NiO into metallic Ni, the formation of amorphous Li_2O, and the reaction of the amorphous SiO_2 coating layer with Li ions to produce Si through $Li_2Si_2O_5$ [44–46]. The second reduction peak at ~1.22 V is attributed to the reduction of amorphous NiO into metallic Ni [47]. However, this peak was not observed in the first discharge process of the hollow NiO@SiO_2 nanopowders obtained after 180 min of oxidation, in which the amorphous NiO layer transformed completely into the crystalline NiO. The reduction peak at ~1.22 V was also absent from the first discharge process of the NiO@SiO_2 nanopowders with filled structures. The good overlap of the CV curves from the second

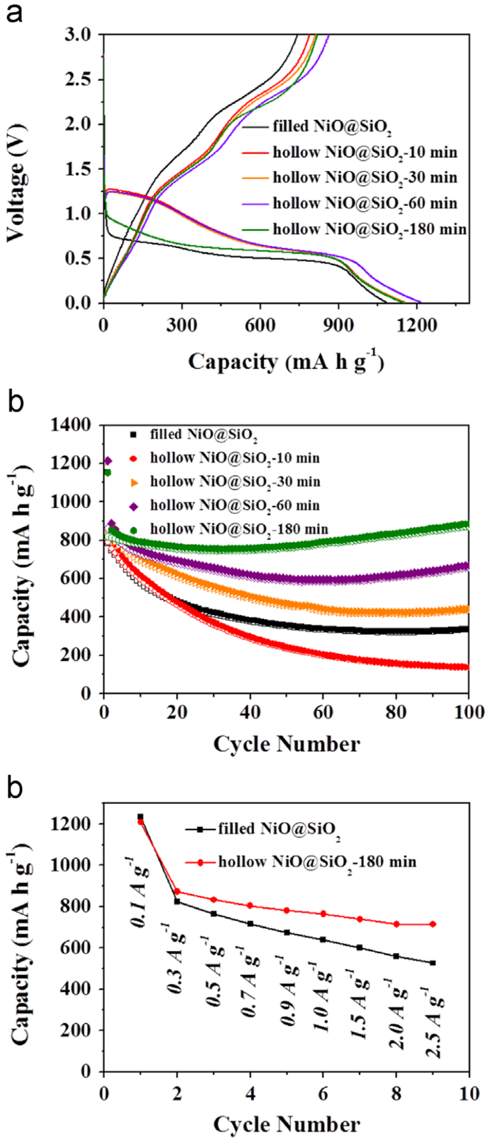

Fig. 10. Electrochemical properties of the filled and hollow NiO@SiO$_2$ nanopowders obtained at various oxidation times: (a) initial charge and discharge curves, (b) cycle performances, and (c) rate performances.

cycle onward revealed the good reversibility of the electrochemical reactions in the hollow NiO@SiO$_2$ nanopowders obtained at an oxidation time of 180 min.

Initial discharge and charge curves (Fig. 10a) of the NiO@SiO$_2$ nanopowders with hollow and filled structures were obtained at a current density of 0.5 A g^{-1}. The curves of the hollow NiO@SiO$_2$ nanopowders obtained at oxidation times below 60 min exhibited distinct plateaus at ~1.2 V in the first discharge process; these plateaus resulted from the reduction of amorphous NiO into metallic Ni [47]. In addition, the initial discharge and charge curves of the hollow NiO@SiO$_2$ nanopowders obtained after 180 min of oxidation had similar shapes as those of the nanopowders with filled structures. However, Li insertion occurred at a slightly higher potential for the hollow NiO@SiO$_2$ nanopowders (with a mean crystallite size of 7.6 nm) than for the filled-structure nanopowders (with a mean crystallite size of 11.2 nm). The hollow NiO@SiO$_2$ nanopowders obtained after oxidation for 10, 30, 60, and 180 min exhibited initial discharge capacities of 1154, 1212, 1215, and 1151 mA h g^{-1}, respectively, and corresponding initial Coulombic efficiencies of 68.3%, 70.4%, 71.0%, and 71.1%, respectively. The initial discharge and charge capacities of the NiO@SiO$_2$ nanopowders with filled structures were 784 and 1156 mA h g^{-1}, respectively. Fig. 10b shows the cycling performances of the hollow and filled-structure NiO@SiO$_2$ nanopowders at a current density of 0.5 A g^{-1}. The cycling performance of the hollow NiO@SiO$_2$ nanopowders exhibited a strong dependence on the oxidation time of the nanoscale Kirkendall diffusion process. In fact, the improved cycling performance of these nanopowders with prolonged oxidation stems from an increase in their crystallinity and mean crystallite size. This finding concurs with the results of Poizot et al., who reported that transition-metal oxides exhibited good electrochemical properties at a certain optimum particle size [48]. Moreover, the hollow NiO@SiO$_2$ nanopowders obtained at oxidation times greater than 60 min exhibited better cycling performance than their filled-structure counterparts. The discharge capacity of the hollow NiO@SiO$_2$ nanopowders obtained after 180 min of oxidation decreased over the first 33 cycles because of the partial destruction of the hollow NiO nanopowders and increased continuously to a value of 886 mA h g^{-1} over the subsequent 67 cycles. This increase in the discharge capacity, which resulted from the formation of a polymeric gel-like film on the active material during cycling, should have also occurred in the other 3 samples. However, continuous destruction of the NiO nanopowders during the long cycles decreased the capacities of the other 3 samples. The hollow NiO@SiO$_2$ nanopowders obtained after 10, 30, 60, and 180 min of oxidation had 100th cycle discharge capacities of 168, 433, 641, and 856 mA h g^{-1}, respectively, and corresponding capacity retentions measured from the second cycle of 20.6%, 49.5%, 72.1%, and 100.4%, respectively. The capacity retention of the NiO@SiO$_2$ nanopowders with filled structure measured from the second cycle was 41.7%. Fig. 10c compares the rate performance of the NiO@SiO$_2$ nanopowders with hollow and filled structures for a stepwise increase in the current density from 0.1 to 2.5 A g^{-1} and with 1 cycle performed at each step. The hollow NiO@SiO$_2$ nanopowders were obtained after 180 min of oxidation. The NiO@SiO$_2$ nanopowders with hollow and filled structures exhibited respective capacities of 1209, 873, 834, 805, 781, 765, 839, 715, and 714 mA h g^{-1} and 1235, 825, 764, 714, 672, 640, 601, and 548 mA h g^{-1} at current densities of 0.1, 0.3, 0.5, 0.7, 0.9, 1.0, 1.5, 2.0, and 2.5 A g^{-1}, respectively; therefore, the hollow NiO@SiO$_2$ nanopowders exhibited better rate performance than the nanopowders with filled structures.

The superior electrochemical properties of the hollow NiO@SiO$_2$ nanopowders compared with those with filled structures were confirmed by EIS measurements (Fig. 11). EIS measurements were performed on the NiO@SiO$_2$ nanopowders with hollow and filled structures before and after 50 cycles. The hollow NiO@SiO$_2$ nanopowders were obtained

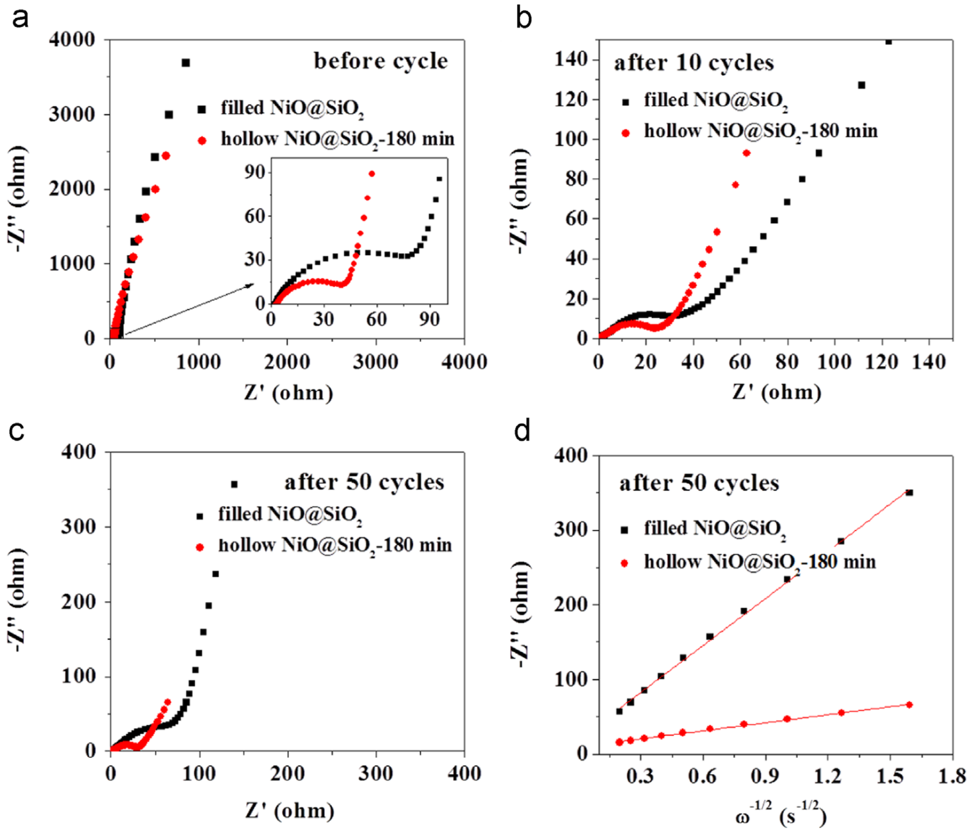

Fig. 11. Electrochemical impedance spectroscopy (EIS) of the filled and hollow nanopowders: (a) Nyquist impedance plots before cycle, (b,c) Nyquist impedance plots after 10 and 50 cycles, and (d) relationships between the real part of the impedance (Z_{re}) and $\omega^{-1/2}$ after 50 cycles.

after 180 min of oxidation. The Nyquist plots consist of compressed semicircles in the medium-frequency range and a line inclined at ~45° to the real axis at low frequencies, which describes the charge-transfer resistance (R_{ct}) of the electrodes and corresponds to Li diffusion within the electrodes, respectively [49–51]. As demonstrated in Fig. 11a–c, the hollow NiO@SiO_2 nanopowders exhibited lower charge transfer resistances before and after cycling than their filled-structure counterparts. In addition, the structural stability of the hollow NiO@SiO_2 nanopowders during cycling resulted in a steady decrease in the charge transfer resistance with an increasing number of cycles. The relationship between the real part of the impedance spectra (Z_{re}) and $\omega^{-1/2}$ (where ω is the angular frequency, $\omega = 2\pi f$) in the low-frequency region, as observed in Fig. 11d, revealed a higher Li-ion diffusion rate for the hollow NiO@SiO_2 nanopowders compared with that of the nanopowders with filled structures [52]. The short Li-ion diffusion length of the 7.2-nm-thick hollow NiO nanopowders resulted in a superior rate performance of these nanopowders compared with that of their filled-structure counterparts.

4. Conclusions

A new process combining flame spray pyrolysis with nanoscale Kirkendall diffusion was developed for the preparation of hollow metal oxide nanopowders. Sintering and particle growth of the metal nanopowders prior to the nanoscale Kirkendall diffusion process was prevented through the application of a SiO_2 coating layer. The reduction process of the core–shell-structured NiO@SiO_2 nanopowders yielded core–shell-structured Ni@SiO_2 nanopowders, and subsequent oxidation resulted in hollow NiO@SiO_2 nanopowders via the nanoscale Kirkendall diffusion process. The electrochemical and physical properties of the hollow NiO@SiO_2 nanopowders were affected by the oxidation time of the nanoscale Kirkendall diffusion process. The electrochemical properties of the hollow NiO@SiO_2 nanopowders were superior to those of the NiO@SiO_2 nanopowders with filled structures. The process developed here can be used to prepare hollow metal oxide@-SiO_2 nanopowders with various compositions for use in numerous applications including energy storage.

Acknowledgments

This work was supported by a National Research Foundation of Korea (NRF) Grant funded by the Korea Government (MEST) (NRF-2015R1A2A1A15056049).

References

[1] M.F. Lin, V.K. Thakur, E.J. Tan, P.S. Lee, Dopant induced hollow $BaTiO_3$ nanostructures for application in high performance capacitors, J. Mater. Chem. 21 (2011) 16500.

[2] J. Du, J. Qi, D. Wang, Z. Tang, Facile synthesis of Au@TiO_2 core–shell hollow spheres for dye-sensitized solar cells with remarkably improved efficiency, Energy Environ. Sci. 5 (2012) 6914.

[3] D. Chen, J. Ye, Hierarchical WO_3 hollow shells: dendrite, sphere, dumbbell, and their photocatalytic properties, Adv. Funct. Mater. 18 (2008) 1922.

[4] J.H. Lee, Gas sensors using hierarchical and hollow oxide nanostructures: overview, Sens. Actuators B-Chem. 140 (2009) 319.

[5] Y. Zhu, T. Ikoma, N. Hanagata, S. Kaskel, Rattle-type Fe_3O_4@SiO_2 hollow mesoporous Spheres as carriers for drug delivery, Small 6 (2010) 471.

[6] G. Zheng, Q. Zhang, J.J. Cha, Y. Yang, W. Li, Z.W. Seh, Y. Cui, Amphiphilic surface modification of hollow carbon nanofibers for improved cycle life of lithium sulfur batteries, Nano Lett. 13 (2013) 1265.

[7] H. Zhang, Z. Zhou, B. Yang, M. Gao, The influence of carboxyl groups on the photoluminescence of mercaptocarboxylic acid-stabilized CdTe nanoparticles, J. Phys. Chem. B 107 (2003) 8.

[8] W. Jin, B. Dong, W. Chen, C. Zhao, L. Mai, Y. Dai, Synthesis and gas sensing properties of Fe_2O_3 nanoparticles activated V_2O_5 nanotubes, Sens. Actuators B-Chem. 145 (2010) 211.

[9] M.M. Rahmana, S.B. Khana, M. Faisalc, M.A. Ruba, A.O. Al-Youbib, A. M. Asiria, Electrochemical determination of olmesartan medoxomil using hydrothermally prepared nanoparticles composed SnO_2–Co_3O_4 nanocubes in tablet dosage forms, Talanta 99 (2012) 924.

[10] K.C. Huang, S.H. Ehrman, Synthesis of iron nanoparticles via chemical reduction with palladium ion seeds, Langmuir 23 (2007) 1419.

[11] W. Wang, M. Dahl, Y. Yin, Hollow nanocrystals through the nanoscale kirkendall effect, Chem. Mater. 25 (2013) 1179.

[12] Y. Yu, X. Yin, A. Kvit, X. Wang, Evolution of hollow TiO_2 nanostructures via the kirkendall effect driven by cation exchange with enhanced photoelectrochemical performance, Nano Lett. 14 (2014) 2528.

[13] B.D. Anderson, J.B. Tracy, Nanoparticle conversion chemistry: Kirkendall effect, galvanic exchange, and anion exchange, Nanoscale 6 (2014) 12195.

[14] S. Krishnamurthy, P.V. Kamat, Galvanic exchange on reduced graphene oxide: designing a multifunctional two-dimensional catalyst assembly, J. Phys. Chem. C 117 (2013) 571.

[15] C. An, J. Wang, C. Qin, W. Jiang, S. Wang, Y. Li, Q. Zhang, Synthesis of Ag@AgBr/AgCl heterostructured nanocashews with enhanced photocatalytic performance *via* anion exchange, J. Mater. Chem. 22 (2012) 13153.

[16] H.J. Fan, U. Gösele, M. Zacharias, Formation of nanotubes and hollow nanoparticles based on Kirkendall and diffusion processes: a review, Small 3 (2007) 1660.

[17] L. Hu, N. Yan, Q. Chen, P. Zhang, H. Zhong, X. Zheng, Y. Li, X. Hu, Fabrication based on the Kirkendall effect of Co_3O_4 porous nanocages with extraordinarily high capacity for lithium storage, Chem. Eur. J. 18 (2012) 8971.

[18] H.K. Han, T.S. Song, J.Y. Bae, L.F. Nazar, H.S. Kim, U. Paik, Nitridated TiO_2 hollow nanofibers as an anode material for high power lithium ion batteries, Energy Environ. Sci. 4 (2011) 4532.

[19] X. Lai, J.E. Halpert, D. Wang, Recent advances in micro-/nano-structured hollow spheres for energy applications: from simple to complex systems, Energy Environ. Sci. 5 (2012) 5604.

[20] Y. Wang, D. Su, A. Ung, J. h Ahn, G. Wang, Hollow $CoFe_2O_4$ nanospheres as a high capacity anode material for lithium ion batteries, Nanotechnology 23 (2012) 055402.

[21] Z. Wang, L. Zhou, X.W. Lou, Metal oxide hollow nanostructures for lithium-ion batteries, Adv. Mater. 24 (2012) 1903.

[22] N.S. Ergang, M.A. Fierke, Z. Wang, W.H. Smyrl, A. Stein, Fabrication of a fully infiltrated three-dimensional solid-state interpenetrating electrochemical cell, J. Electrochem. Soc. 154 (2007) A1135.

[23] Y. Yao, M.T. McDowell, I. Ryu, H. Wu, N. Liu, L. Hu, W.D. Nix, Y. Cui, Interconnected silicon hollow nanospheres for lithium-ion battery anodes with long cycle life, Nano Lett. 11 (2011) 2949.

[24] C. Niu, J. Meng, C. Han, K. Zhao, M. Yan, L. Mai, VO_2 nanowires assembled into hollow microspheres for high-rate and long-life lithium batteries, Nano Lett. 14 (2014) 2873.

[25] A. Vu, Y. Qian, A. Stein, Porous electrode materials for lithium-ion batteries – How to prepare them and what makes them special, Adv. Energy Mater. 2 (2012) 1056.

[26] J. Lian, X. Duan, J. Ma, P. Peng, T. Kim, W. Zheng, Hematite (α-Fe_2O_3) with various morphologies: ionic liquid-assisted synthesis, formation mechanism, and properties, ACS Nano 3 (2009) 3749.

[27] H.B. Lin, H.B. Rong, W.Z. Huang, Y.H. Liao, L.D. Xing, M.Q. Xu, X. P. Li, W.S. Li, Triple-shelled Mn_2O_3 hollow nanocubes: force-induced synthesis and excellent performance as the anode in lithium-ion batteries, J. Mater. Chem. A 2 (2014) 14189.

[28] Y.M. Lee, M.R. Jo, K.S. Song, K.M. Nam, J.T. Park, Y.M. Kang, Hollow Sn–SnO_2 nanocrystal/graphite composites and their lithium storage properties, ACS Appl. Mater. Interfaces 4 (2012) 3459.

[29] Y. Yin, R.M. Rioux, C.K. Erdonmez, S. Hughes, G.A. Somorjai, A. P. Alivisatos, Formation of hollow nanocrystals through the nanoscale Kirkendall effect, Science 304 (2004) 711.

[30] R.K. Chiang, R.T. Chiang, Formation of hollow Ni_2P nanoparticles based on the nanoscale Kirkendall effect, Inorg. Chem. 46 (2007) 369.

[31] H.J. Fan, M. Knez, R. Scholz, D. Hesse, K. Nielsch, M. Zacharias, U. Gösele, Influence of surface diffusion on the formation of hollow nanostructures induced by the Kirkendall effect: the basic concept, Nano Lett. 7 (2007) 993.

[32] A.A.E. Mel, M. Buffière, P.Y. Tessier, S. Konstantinidis, W. Xu, K. Du, I. Wathuthanthri, C.H. Choi, C. Bittencourt, R. Snyders, Highly ordered hollow oxide nanostructures: the Kirkendall effect at the nanoscale, Small 9 (2013) 2838.

[33] H.B. Wu, J.S. Chen, H.H. Hng, X.W. Lou, Nanostructured metal oxide-based materials as advanced anodes for lithium-ion batteries, Nanoscale 4 (2012) 2526.

[34] J.H. Kim, Y.J. Hong, B.K. Park, Y.C. Kang, Nano-sized $LiNi_{0.5}Mn_{1.5}O_4$ cathode powders with good electrochemical properties prepared by high temperature flame spray pyrolysis, J. Ind. Eng. Chem. 19 (2013) 1204.

[35] S.H. Choi, Y.N. Ko, J.K. Lee, B.K. Park, Y.C. Kang, Core shell-structure Ag-$BaTiO_3$composite nanopowders prepared directly by flame spray pyrolysis, Mater. Chem. Phys. 140 (2013) 266.

[36] G.D. Park, S.H. Choi, Y.C. Kang, Electrochemical properties of ultrafine TiO_2-doped MoO_3 nanoplates prepared by one-pot flame spray pyrolysis, RSC Adv. 4 (2014) 17382.

[37] J.H. Kim, D.S. Jung, J.K. Lee, Y.C. Kang, Sintering characteristics of nano-sized Ag-Pd-glass composite powders with high Pd content, J. Mater. Sci. 47 (2012) 7090.

[38] P. Pawinrat, O. Mekasuwandumrong, J. Panpranot, Synthesis of Au–ZnO and Pt–ZnO nanocomposites by one-step flame spray pyrolysis and its application for photocatalytic degradation of dyes, Catal. Commun. 10 (2009) 1380.

[39] W.Y. Teoh, R. Amal, L. Mädler, Flame spray pyrolysis: an enabling technology for nanoparticles design and fabrication, Nanoscale 2 (2010) 1324.

[40] H.Y. Koo, J.H. Yi, J.H. Kim, Y.N. Ko, D.S. Jung, Y.C. Kang, J.H. Lee, Conductive silver films formed from nano-sized silver powders prepared by flame spray pyrolysis, Mater. Chem. Phys. 124 (2010) 959.

[41] S.H. Choi, J.H. Lee, Y.C. Kang, One-pot rapid synthesis of core–shell structured NiO@TiO_2 nanopowders and their excellent electrochemical properties as anode materials for lithium ion batteries, Nanoscale 5 (2013) 12645.

[42] J.G. Railsback, A.C. Johnston-Peck, J. Wang, J.B. Tracy, Size-dependent nanoscale kirkendall effect during the oxidation of nickel nanoparticles, ACS Nano 4 (2010) 1913.

[43] X.H. Huang, J.P. Tu, C.Q. Zhang, F. Zhou, Mesoporous NiO nanosheet networks as high performance anodes for Li ion batteries, Electrochim. Acta 55 (2010) 8981.

[44] N. Yan, F. Wang, H. Zhong, Y. Li, Y. Wang, L. Hu, Q. Chen, Hollow porous SiO_2 nanocubes towards high-performance anodes for lithium-ion batteries, Sci. Rep. 3 (2013) 1568.

[45] W.S. Chang, C.M. Park, J.H. Kim, Y.U. Kim, G.J. Jeong, H.J. Sohn, Quartz (SiO_2): a new energy storage anode material for Li-ion batteries, Energy Environ. Sci. 5 (2012) 6895.

[46] Q. Sun, B. Zhang, Z.W. Fu, Lithium electrochemistry of SiO_2 thin film electrode for lithium-ion batteries, Appl. Surf. Sci. 254 (2008) 3774.

[47] H. Qiao, N. Wu, F. Huang, Y. Cai, Q. Wei, Solvothermal synthesis of NiO/C hybrid microspheres as Li-intercalation electrode material, Mater. Lett. 64 (2010) 1022.

[48] P. Poizot, S. Laruelle, S. Grugeon, L. Dupont, J.M. Tarascon, Nano-sized transition-metal oxides as negative-electrode materials for lithium-ion batteries, Nature 407 (2000) 496.

[49] M.S. Park, Y.M. Kang, G.X. Wang, S.X. Dou, H.K. Liu, The effect of morphological modification on the electrochemical properties of SnO_2 nanomaterials, Adv. Funct. Mater. 18 (2008) 455.

[50] Y.N. Ko, S.B. Park, K.Y. Jung, Y.C. Kang, One-pot facile synthesis of ant-cave-structured metal oxide–carbon microballs by continuous process for use as anode materials in Li-ion batteries, Nano Lett. 13 (2013) 5462.

[51] G.D. Li, L.Q. Xu, Q. Hao, M. Wang, Y.T. Qian, Synthesis, characterization and application of carbon nanocages as anode materials for high-performance lithium-ion batteries, RSC Adv. 2 (2012) 284.

[52] Y. Shi, J.Z. Wang, S.L. Chou, D. Wexler, H.J. Li, K. Ozawa, H.K. Liu, Y.P. Wu, Hollow structured Li_3VO_4 wrapped with graphene nanosheets in situ prepared by a one-pot template-free method as an anode for lithium-ion batteries, Nano Lett. 13 (2013) 4715.